Development of a Ring PET Insert for MRI

Chris Bauer, Alexander Stolin, James Proffitt, Peter Martone, Julie Brefczynski-Lewis, James Lewis, Janusz Hankiewicz, Ray Raylman, and Stan Majewski

Abstract–Our research group constructed a 12-module PET detection ring composed of Hamamatsu multi-pixel photon counter (MMPC) silicon photomultiplier (SiPM) detectors placed in a ring that is fully MRI compatible. This brain imager can be placed around the head of a patient (clinical setting) or subject (research setting) and allow for comfortable upright imaging. However, an alternative way to use this device, as enabled by the technology, is to indeed scan individuals in the supine position in conjuncture with current MRI systems. This PET prototype is able to image simultaneously as the MRI scan is occurring, thus maximizing co-registration and the accuracy of the assignment of metabolically active voxels to their anatomically correct counterparts as identified by the MR image. In this study, we first conducted some basic instrumentation tests to ensure the device was functioning properly outside of the MRI, and additionally scan some phantoms (Derenzo; Hoffman Brain) to assess the quality in which our brain imager is able to produce adequate images. After these initial studies, we conducted multiple different experiments inside a 3 Tesla MRI in order to see how the magnetic field would influence the operation of the PET imager and vice versa. Through simultaneous PET/MRI scanning of a Hoffman brain phantom filled with F^{18} radioactivity and water, it was shown that the quality of the MR image was largely unaffected by the PET imager. Furthermore, although the quality of PET imaging was affected by the RF pulsing, an acceptable PET image was nevertheless produced. As we discuss following the results, the success of this study shows that our brain imager is indeed MR compatible, and that next generation devices based on its concepts will continue to improve combined PET/MRI functionality. As two of the major advantages of this imager are the potential for low-dose scanning and its adaptability to any MRI scanner, this study suggests that PET/MRI brain imaging with low dose is in principle possible using an insert which could be adapted to any MRI scanner, using standard RF coils for that scanner.

C. Bauer is with West Virginia University, Morgantown, WV 26505 USA (e-mail: cbauer5@mix.wvu.edu).

A. Stolin is with West Virginia University, Morgantown, WV 26505 USA (e-mail: astolin@hsc.wvu.edu).

J. Proffitt is with Ait Technologies, Newport News, VA 23606 USA (e-mail: jproffitt@ait-instrument.com).

P. Martone is with West Virginia University, Morgantown, WV 26505 USA (e-mail: pmartone@hsc.wvu.edu).

J. Brefczynski-Lewis is with West Virginia University, Morgantown, WV 26505 USA (e-mail: jblewis@hsc.wvu.edu).

J. Lewis is with West Virginia University, Morgantown, WV 26505 USA (e-mail: jwlewis@hsc.wvu.edu).

J. Hankiewicz is with the University of Colorado, Colorado Springs, CO 80918 USA.

R. Raylman is with West Virginia University, Morgantown, WV 26505 USA (e-mail: rraylman@hsc.wvu.edu).

S. Majewksi is with West Virginia University, Morgantown, WV 26505 USA (e-mail: smajewski@hsc.wvu.edu).

I. INTRODUCTION

Positron emission tomography (PET) has existed since the early 1960's and was the first real attempt to image organs and biological systems *in vivo* on the molecular level using radiotracers [1]. Although this technology has been continuously improved upon and more efficient scanners have been produced throughout the decades, the widespread development of organ-specific PET imaging has been limited thus far. Despite a lack of large-scale organ-specific development of such imagers, our group has been able to develop a brain-dedicated low-dose PET imager largely based on other organ-specific research and existing prototypes, which has the capacity to image human subjects in the upright position or simultaneously with an MR imager.

In recent years there have been a few dedicated PET brain imagers constructed. The Siemens' HRRT, Hamamatsu's SHR-12000, and Photo Diagnostic's NeuroPET/CT are excellent examples of how well these devices can perform (Fig. 1.). Philips is developing technology which could be used as a time-of-flight PET brain imager with good timing resolution (~275 psec FWHM) and energy resolution (down to 11% FWHM @511 keV) [2]. Preliminary results demonstrate that TOF information at the achieved timing resolution level produces improvements in image contrast even in objects as small as 7cm. However, thus far the current brain-specific imagers and prototypes produced have not allowed for freedom of movement, upright imaging, and MRI compatibility in combination.

Fig. 1. Displayed here is some of the relevant prior art. From left to right: Siemens' HRRT, Photo Diagnostic Systems' NeuroPET/CT imager; Philips Digital Photon Counting's TOF PET; the PET-Hat; and the WVU Helmet_PET (different, yet similar to the ring described here) in non-MRI, upright form.

There are, however, a few such PET/MRI brain systems which incorporate some of these facets that are currently in development. Three examples are shown in Fig. 2. One incorporates an RF coil with a PET ring [3, 4]. The second, the WVU Helmet_PET imager (not the ring described in this study), employs a standard RF coil which is placed between the object subject to imaging and the ring modules. Additionally, there is no active circuitry in the modules except for the SiPM photodetectors. The preferred coil type for this device is one of the flexible standard coils from the package of

coil attachments included with many MRI systems. The third example is the Sogang University PET insert (similar to the WVU Helmet_PET) which has no electronics inside the magnet bore, however the PET ring is large enough to be placed outside the standard birdcage RF head coil at the expense of lower efficiency and/or higher cost, complexity, and weight [5-8]. Sogang system's electronics readout has no multiplexing as in the operation of Helmet_PET, and overall is larger and more expensive, but also more complex. In the brain imager used in this study, the front-end amplifiers are placed in the modules of the ring along with the scintillator and photodetectors, and only the basic necessary control electronics (placed on a small MR-compatible cart) stay inside the MRI room. The remaining electronics, data acquisition system (DAQ) and computer with DAQ and processing software are placed in a wheeled cabinet/rack outside in the MRI operator room. Screened cables connect the electronics inside the MRI room with the rack/cabinet, exiting the MRI room via standard wall port. The RF (flexible) coil is placed inside the ring and preferentially extends past the edge of the PET insert.
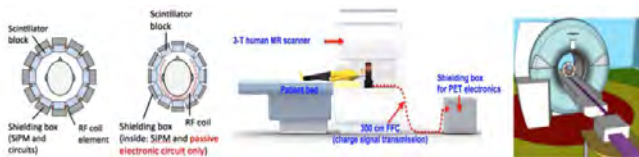

Fig. 2. Additional recent prior art is displayed here. Left: The RF coil is integrally built into the PET ring. Second: WVU Helmet_PET concept: No active circuitry except SiPM light sensors with the RF coil placed between the object to image and the ring modules. Third: The Sogang University (Korea) brain PET MRI insert concept. Right: Our novel concept in this study, which has three important differentiators: (1) the ring in our design is closely following the patient's head, (2) we do not use a specially built RF coil accompanying the PET ring nor the standard brain coil. We use a standard flexible RF coil provided with the MRI scanner, allowing for much tighter structure of the ring. (3) Our amplifiers are in the detectors heads providing better PET operation.

The initial concept of a wearable PET device, PET-Hat [9, 10] originally postulated that the patient sits in a chair with a single ring of 16 detector modules based on position sensitive photomultiplier tubes (PSPMTs). While compact in comparison to standard PMTs, PSPMTs are still bulky enough that the combined size and weight of the resulting PET-Hat ring imager requires a counterbalanced mechanical support to allow the ring to follow small movements of the patients' heads. This initial concept was taken to the next stage by the West Virginia University Center for Advanced Imaging (WVU-CAI) group by replacing the PSPMTs with silicon photomultipliers (SiPMs). Both the Helmet_PET imager and the brain imager used in this study are very tight rings (inner diameters of 20-22cm) of 12 Hamamatsu SiPM based PET detector modules covering about 5cm of the brain vertically. Since the devices utilize the highly sensitive SiPM technology and are much closer to the head, the devices are capable of low-dose imaging. The rings can be repositioned to see the desired part of the brain, and Helmet_PET in particular is suspended from above. In order to adjust Helmet_PET in

respect to the patient, the prototype may be lowered and attached in a helmet style to the patient's head [11]. This design allows the patient to potentially sit, stand, move, or even exercise while being imaged. However, this design also permits the prototype to become detached from the overhead frame and function as an MRI insert as stated previously. Within the MRI, this system arrangement is extremely patient-friendly allowing for head movements while the PET ring stays co-registered with the brain.

Although Helmet_PET and the current brain imaging system has many advantages such as MR compatibility and low dose imaging, the current tight geometry of the ring surrounding the head/neck that is required to achieve high efficiency (and low injection dose), compactness, low weight, and low cost introduces cracks in the ring between the modules. This limits angular sampling, resulting in artifacts being present in the reconstructed images. However, it is our plan to implement the best correction algorithms in future next-generation devices in order to minimize these effects. Of course, next generation imagers built by our group will also contain more modules thus also minimizing the effects in a different way. It may also be possible for us to model the detector response, which would greatly enhance the removal of artifacts, the level of image normalization, and overall image quality. However, at present we have been using a simplified yet efficient image correction method developed at the WVU Center for Advanced Imaging, which is performed by image division of the slices obtained from the imaged object (such as a phantom or a patient's head) by the corresponding slice images of a cylindrical "flood" phantom (a cylinder comprising the entire field of view of the imager, which is filled with a fluid with a uniform concentration of radioactivity). As can be seen in Figure 3, the results of this image normalization are satisfactory. This uniformity correction accounts for not only the geometrical response matrix of the detectors but also for the bulk of the 511 keV annihilation gamma absorption effects. The geometrical response matrix includes the detector response due to the fact that the detector ring is "broken" into modules-pieces with gaps between the modules. In addition, it corrects for the imperfections in the detectors or the errors in the calibration procedure.
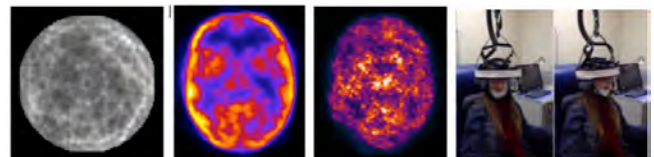

Fig. 3. Examples of preliminary data obtained with the WVU Helmet_PET imager. Flood image obtained with a 185 mm diameter by 5mm high cylinder filled with F18 water solution (left: *Note image artifacts due to breaks between detector modules*.) Brain phantom image after correction by the flood image at left (second from left). Example of the first human images (middle). This is a two millimeter slice of a volunteer patient brain obtained in a 10 minute scan 4 hours after standard ~10 mCi F18-FDG injection. The images are corrected for absorption. Despite artifacts seen in the flood image at left, the phantom and patient images are properly corrected. Two frames from a video at right show that the WVU Helmet-PET can follow the rotating

head movements. The same mobility features will be implemented in our current wearable PET brain imager

Our new prototypes are novel in a myriad of different ways. Firstly, and most appropriately for the purposes of this paper, they are fully MRI-compatible and can easily function as an insert. In conjunction with this functionality, standard flexible RF coils can be wrapped around this prototype in order to shield the MRI from an electrical noise generated from the PET insert. In addition, the applications of these flexible coils could replace the standard "bird cage" or head coil used for MRI brain imaging and in the process provide a stronger and potentially more accurate MRI image. An additional novelty, not specific to the MRI compatibility of these prototypes, is the fact that these imagers operate with extremely low radioactive dose. This low-dose capability is partially due to the fact that the imagers are much closer to the head than standard PET/CT, thus increasing the overall efficiency our prototypes. The second reason why the device is low-dose is inherent in the SiPM technology, which is much more sensitive overall although it does suffer from a poor signal to noise ratio. Ultimately, these two reasons result in the prototypes operating at approximately 10% of the standard dose that PET/CT uses, which has important longitudinal research applications and allows for repeated PET/MRI scans within a small period of time if necessary. It should be noted, however, that the low dose imaging is not incredibly useful if one wishes to view small structures with fine resolution; the low dose is more for pattern imaging. The final novelty of these devices, as mentioned previously in this paper, is that they are brain-dedicated. Although standard PET/CT provides overall better quality of the entire body (since it is a fully-developed, professional instrument compared to our first generation prototype), these new prototypes have the capability of obtaining more precise images of the head in subsequent developmental stages. We believe that Helmet_PET and the current brain imager are one of the first instruments in the world to combine brain-dedicated low-dose imaging with SiPM technology in the form of an MRI-compatible PET insert with no dedicated RF coil.

The purpose of the current study was to repeat some of the basic instrumentation measurements on our new brain imager which we have already investigated in order to ensure proper function of Helmet_PET outside of the MR scanner. In these experiments, we report energy spectra results, coincidence detection results on individual detectors, as well as coincidence detection on the entire image. Additionally we report spatial resolution at various points within the brain imager's field of view, timing resolution, and the effect of acquisition rate on the reconstructed image quality. We also look at the effect of temperature on the system's efficiency, as SiPMs are known to very sensitive even at ambient temperatures. We then verify our normalization procedure by showing that indeed a very simple yet effective method of image division by our "flood" phantom can eliminate most artifacts. The final experiments we conduct outside the MRI involves the imaging of a realistic Hoffman brain phantom,

which represents the image quality if a real brain were imaged.

In the next phase of this study, we proceed to show results collected from within the MRI scanner. We first demonstrate that our current brain imager has very little impact on the images generated from MRI. After this initial confirmation, we thus hypothesized that the Hoffman brain phantom could be imaged using simultaneous PET/MRI scanning, and that the images from both modalities would be of reasonable quality while showing no obvious artifacts or distortions. The results from this study indicate the feasibility of simultaneous PET/MR imaging in subsequent prototypes, and suggest that multiple positive aspects of this imager, such as MR-compatibility and low-dose imaging, can be synergistically combined to improve overall the quality and applicability of PET brain imaging.

II. MATERIALS AND METHODS

A. Materials

The modules for the this prototype brain PET imager were built using 5x10 arrays of 3mm Hamamatsu (Hamamatsu city, Japan) MPPCs [4] coupled to arrays of 16x32 LYSO pixels with 1.5mm pitch and 10mm thick from Proteus (Chagrin Falls, OH) [12]. The considerations were the compactness, weight, cost and depth of interaction (DOI). However, since the scintillator was only 1 cm thick, the impact of DOI (DOI was not corrected for) was limited. The Helmet_PET is built with custom built from ~1" silicon photomultiplier (SiPM) detector modules, each based on 5x5 arrays = 25 total of ~3mm Hamamatsu S10362-33-050P MPPCs, specifically made for WVU. The 1" modules can be butted together to form larger modules, for example a 2x2 module configuration. In the current system it is only a 1x2 module configuration. These newly assembled larger modules can be used as compact, MRI compatible "plug-in" replacements for the H8500/H9500 flat panel position sensitive photomultiplier tubes (PSPMTs). After the initial evaluation studies confirming that our technology was functional, the next phase of the project was to equip the detector modules with resistive readout and assemble them into a helmet type head imager in order to perform tests with all module functioning together.

The imager used in this study has the amplifiers directly next to the electronics and photodetectors on the modules themselves, as opposed to other rings systems in our laboratory (Helmet_PET). A charged division readout from AiT Instruments (Newport News, VA) [13] which employed 4 channels per module was implemented. The amplified detector signals were digitized in the FPGA USB2 DAQ system of integrating ADCs from AiT Instruments [14]. The initial studies were performed with a small-size 8-module prototype before upgrading it to the full size 12 module ring. Read-out software was implemented using the Java programming language with an overlaying user interface provided by a Kmax scientific programming package from Sparrow Corporation (Port Orange, FL) [15].
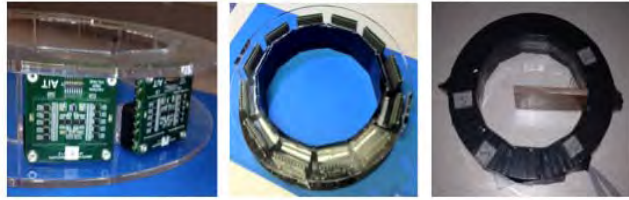
B. Detector Construction/Calibration

Fig. 4. Assembly stages of the PET ring using the same type of acrylic ring mount as used in the WVU's Helmet_PET system. Shown at left are the back end of the modules in a pre-construction stage. Each module has charged division circuitry and front-end amplifiers on board, made by AiT Instruments. Right: fully assembled light tight ring used for validation studies.

After the initial construction the ring was assembled and wrapped in black tape to produce a light tight imager for use in our studies (Fig.4). Each detector head was connected to the power supply and control box by a ribbon cable. This control box provides the bias voltage for the SiPMs, transfers the signals to an ADC, and produces a sum signal. This sum signal is then sent to a Mesytec MST_MCFD-16 discriminator with coincidence logic which provides the trigger for the ADC. The bias voltage was adjusted so that each head gave approximately the same output amplitude sum signal as measured on an oscilloscope. The average value was 73.6 volts.

C. Reconstruction and Image Processing

Images were reconstructed using custom-written software. Our reconstructions in these experiments generally used 1x1x1 millimeter voxels and iterative reconstruction for 10 iterations. Reconstructed images were displayed using Image J. Analysis and measurements of the reconstructed images were likewise assessed using Image J.

III. EXPERIMENTAL DESIGN

A. Pixel Separation and Calibration

Before engaging in subsequent whole-image testing, we first wished to produce a raw image using a program written in Kmax [15] to verify that all the crystal pixels could be seen on the face of the detector and that they were easily separated (Fig. 5). Six Na22 point sources were placed in the center of the ring and the resulting events were acquired. The Mesytec trigger module was set to record all events within the energy window, not necessarily those in coincidence. After the pixels were separated and defined, a pixel map calibration occurred using an Image J plugin in order to link the recorded events on the computer screen in each pixel to that pixel's relative position in the physical crystal array. This plugin then saved the calibration and re-inserted it into the data acquisition software.

B. Energy Calibration and Spectra

After the crystal map calibration, energy spectra were acquired for each pixel to find the location of the 511 keV photopeak for each pixel. We have included 4 representative energy spectra graphs in Fig. 6 which correspond to ROIs identified in Fig. 5. After the energy spectra was acquired a multiplication table was then produced to normalize the 511 keV photopeak for each crystal to the same amplitude (Fig. 7). In addition, we utilized a cylindrical phantom 185 mm in diameter with uniform radioactive concentration and obtained the annihilation events for all the detector heads in order to observe how uniform the individual detectors registered events. This information was subsequently used in order to normalize for uniformity across all modules in the ring.

C. Linearity and Spatial Resolution

In order to study spatial linearity, we placed six ~1mm point Na22 sources in a line staring with a central point, and extending outward at 20 mm, 40mm, 60mm, 80mm, and 90mm from the center. We also probed several different regions of the ring, as shown in Fig. 8. Spatial resolution of the points and the linearity in reconstructed space was recorded.

D. Timing Resolution

We selected two pairs of opposite modules in the ring and measured the coincidence timing resolution using sum signals from these two modules (with 50 MPPC units each) triggering two corresponding channels from a NIM standard model 715 Timing Discriminator from Phillips Scientific and an ACAM-Messelectronic AM-GPX time to digital converter (TDC) system. Data was collected for approximately 30 minutes until the timing resolution was clearly defined.

E. Rate Capability Tests

In a rate capability study of the acquisition electronics performed for the Helmet-PET imager we reached a rate limit of 250 kHz, which was imposed by the data throughput of the USB2 link between the 64ch ADC AiT Instruments module and the computer. However, to establish the true useful rate capability of the system, we tested the imaging performance versus coincidence trigger rate in these experiments. A thin walled 185mm inner diameter acrylic cylinder filled with F18-water solution was imaged at different times post-preparation, hence sampling the rate capability of the system at various different rates based on the radioactive concentration at that time point. The rate changed according to the half-life constant of F^{18}, which is about 109.8 minutes. We examined the reconstructed images of the uniform cylinder phantom and checked to see if any artifacts were visible. Indeed, it is our opinion that it is safe to image at the corresponding rates if no artifacts were present in the uniform phantom.

F. Temperature Measurements

The detector operation and calibration was primarily tested at room temperature (23.5 ºC). However, we also tested the detector at two lower temperatures: 16.7 ºC and 14.5 ºC. In this case, the full ring was put inside a refrigerated chamber and stabilized for several hours. The actual temperature inside the detector ring was not measured and, due to the heating of the low power amplifiers, was slightly higher than the ambient

temperature. After about half an hour powered in the lab, there was no change in the position of the 511 keV photopeak over time at the various temperatures tested. At these temperatures the energy resolution, efficiency and image quality after reconstruction were all assessed.

G. Uniformity Calibration and "Flood" Correction

As seen in Fig. 14, the tight ring detector structure of this brain imager with gaps of about 8mm and no DOI correction produces response artifacts. In order to correct for that, a novel solution was found by researchers at WVU. A 185 mm diameter plastic cylinder is placed inside the PET ring and filled with an ^{18}F water solution of uniform concentration, and data is collected for multiple hours. Although the image that results from said data collection is full of artifacts and non-uniformities, it is representative of the structural flaws of the device and mimics a primitive calibration technique if used correctly. In these experiments we verify that our methodology, though imperfect and simple, can be highly effective for practical purposes. Indeed, we show that although the normalization or "flood" phantom is full of non-uniformities induced by geometry, and that a smaller phantom of interest is full of non-uniformities induced by geometry, the division of the two images results in the smaller phantom of interest being uniform and artifact-free. The smaller phantom of interest was 135 mm in diameter, and was imaged at the same four rates as the larger flood phantoms by which they were divided to produce an image (Fig. 14).

H. Studies with Phantoms

We studied the operation of our prototype imager with a small Derenzo phantom and a multi-compartmental brain phantom. The images were reconstructed with and without absorption correction and then "normalized" by the respective responses from a uniform cylinder "flood" phantom with 185mm inner diameter filled with F18 water solution.

I. MRI-Operation

Our initial plans did not include studies of the ring as a PET insert in MRI, but only as a stand-alone mobile PET imager. However, with the growing interest in PET/MRI hybrid systems, we added a very preliminary study in which we inserted the Phase I ring in a 3 Tesla Siemens MRI scanner to test the effect of the PET scanner on the MRI images. In our unique approach, we used standard flexible coils from a coil kit to demonstrate that we can obtain high S/N MRI images of a brain phantom when the coils were placed inside a powered PET ring (Fig. 17, 18). During image acquisition with MPRAGE, T1, and T2 pulse sequences we found there were strong pulses induced by MRI picked up in the PET signal cables because they were unshielded ribbon cables (Fig. 19).

IV. RESULTS

A. Pixel Separation and Calibration

Each detector head shows up in our image as two slightly separated vertically stacked arrays of pixels. The small separation is due to the optics of the two crystal array assemblies butted against each other and not the fact that there are two arrays of SiPMs. In the image, the top and bottom edge pixels are clearly separated, however, the left and right edge pixels tend to overlap which is due to centering the crystal arrays on the 1x2 array of SiPMs. With a full 2x2 array of SiPMs all edge pixels will be clearly separated. This raw image was then used to make a crystal map calibration to map the computer image to the physical location of each crystal pixel.
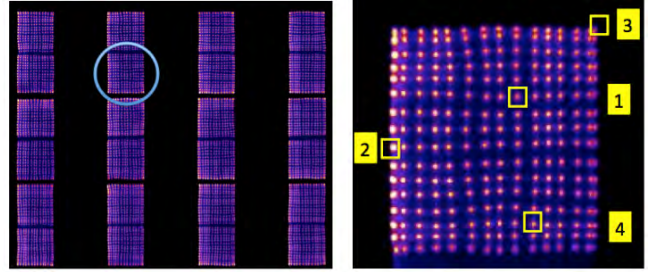
Fig. 5. Raw images for all 12 modules of the ring (left, 1x2 SiPM modules), and one of the modules, circled at left, showed with four selected pixels. All the LYSO pixels, except the left and right edge regions, are very well separated.

B. Energy Calibration and Spectra

Results for the energy calibration and spectra are shown below. The energy resolution was shown to be good enough for the purposes of our experiments, and all detectors remained relatively uniform in regards to gain (Fig. 7, right).
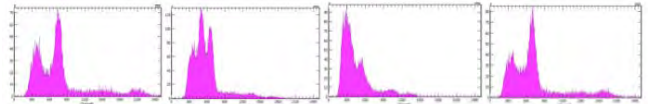
Fig. 6. Energy spectra measured with Na22 sources for the four LYSO pixels selected above in Fig. 5, and marked 1-2-3-4 from left to right. Energy resolution FWHM measured at the 511 keV photopeak: 17.5% (Pixel 1), and 20.0% (Pixel 4). The pixel 2 region has two overlapping pixels producing the two-peak structure, and the edge pixel 3 has many low energy pulses from scattered gammas.
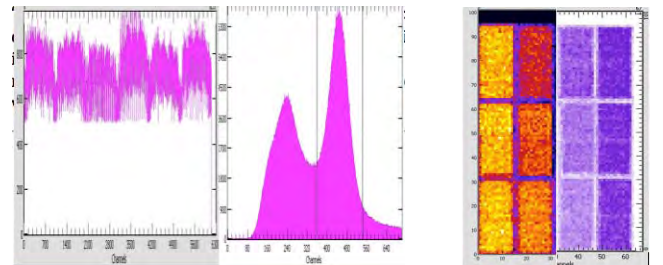
Fig. 7. Left: energy normalization lookup table. Middle: the normalized energy spectrum for the entire detector showing an energy resolution = 16.8% FWHM. Right: flood images measured for the 12 modules shown separately for two six detector sectors obtained for the energy window as shown in the normalized energy spectrum.

C. Linearity and Spatial Resolution

The measured uniformity response of the detector in these experiments shows no evidence of warping or spatial distortion (Fig. 8 and Fig. 9). This will be more fully studied

with our full prototype and we will potentially introduce additional calibration/correction maps to correct for any residual non-linearities. Figure 11 shows that spatial resolution changes from about 2mm FWHM in the center to about 4.5mm 9 cm from the center in practically any direction, either towards the detector module centers or the gap regions. At a distance of 6 cm the resolution is still at the ~3mm FWHM level.

Fig. 8. Set of six 1mm point Na22 sources placed in a line with 20, 20, 20, 20, and 10mm center-to-center spacing. The line of sources was placed in four positions to probe the spatial resolution and linearity response (left-to-right: Position 1,2,3,4).

Fig. 9. Reconstructed sets of six aligned point sources in four positions (left-to-right: Position 1,2,3,4) as in Fig 9.
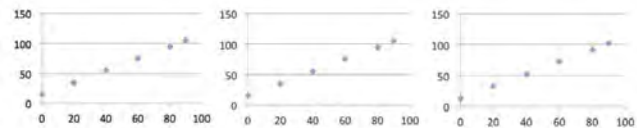
Fig. 10. Plots of the distance from the center of the ring (horizontal scale in mm) verses relative reconstructed positions (vertical scale in pixels) of the point sources in Figure C5, for positions 1 (left), 3 (center) and 4 (right). The relationship is quite linear and thus there is no evidence of spatial compression at the edges.
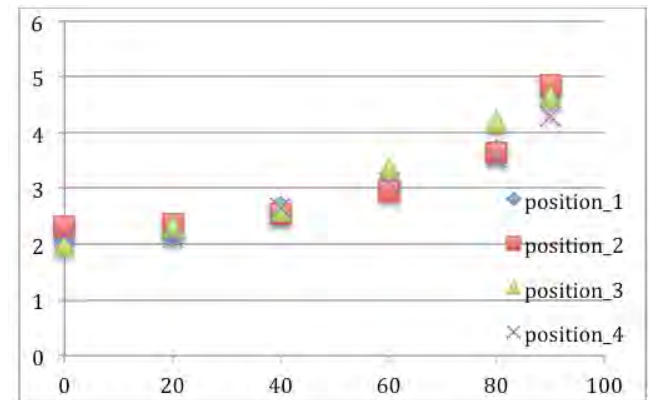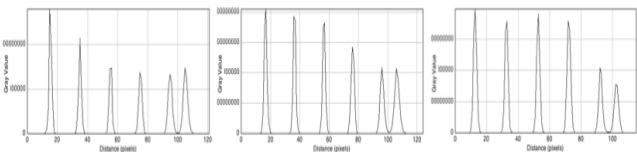

Fig. 11. Above: plots through the reconstructed six point sources, for positions 1 (left), 3 (second) and 4 (third). The plots demonstrate a decrease of spatial resolution towards the edges (greater FWHM) but there is no evidence of spatial compression. The plot on the bottom shows the FWHM spatial

resolution (vertical scale in mm) for the point sources versus the distance in mm from the ring center (horizontal scale).

D. Timing Resolution

A time resolution of 3.5 nanoseconds FWHM was measured which is consistent with the electronics optimized for S/N performance and not for timing (Fig. 12). The timing resolution will continue to be improved upon in subsequent prototypes.
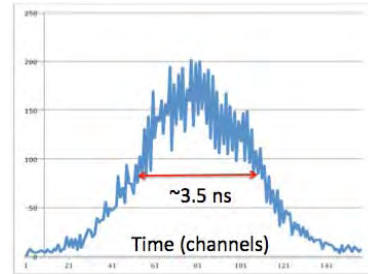

Fig. 12. Coincidence time curve between a pair of opposite modules in the ring showing a FWHM of ~3.5 nanoseconds.
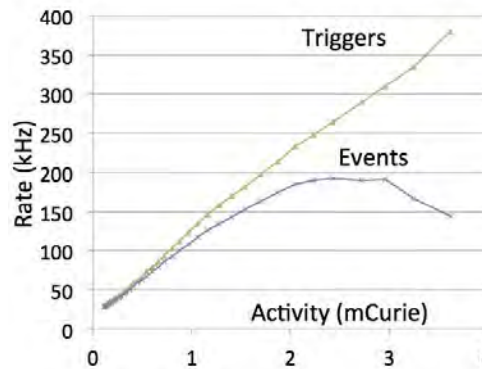
E. Rate Capability Tests

Fig. 13. Rate test showing the number of triggered events collected in a single 64 channel AiT Instruments ADC box and number of events transferred to the acquisition software (Kmax 8.2.2). The phantom consisted of an F18 source in water in a 185mm diameter cylinder placed in the brain PET imager.

Up to a rate of about 10 kHz, the system's imaging response is linear (Fig. 13). From the previously executed DAQ rate test we conclude that this limitation is entirely coming from the radiation flux per unit detector surface. Thus, taking into account that the detector's angular coverage is only ~half of what we will have in the next generation device, a two times larger detector will give four times higher coincidence rate at the same surface rate. The expected rate capability is therefore about 50 kHz *which is consistent with the goal of low-dose imaging* at a 10% of standard dose injection. This reasoning is supported by tests with WVU's version of the Helmet-PET which has a full ring and a rate limit of about 60 kHz. Although the electronics are not identical, they are very similar.

F. Temperature Measurements

As expected, the amplitudes increased at a rate of about 6% per degree indicating an increase in efficiency and the energy

resolution improved from 17.5% at 23.5 ºC to 13.5% at 14.5 ºC. There was no noticeable change in the quality of the images when the energy was normalized for that temperature.

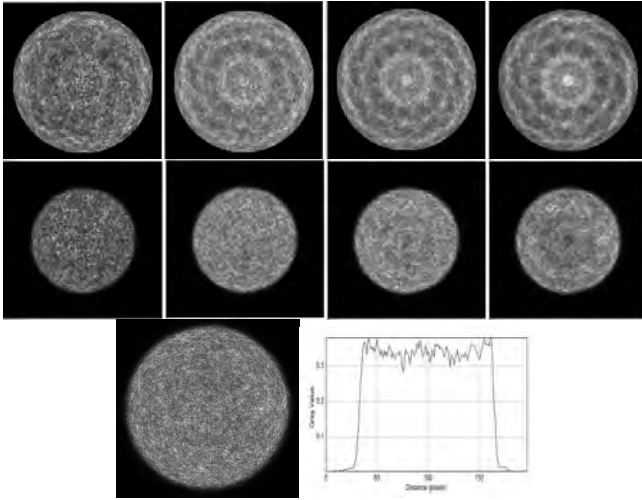### G. Uniformity Calibration and "Flood" Correction

Fig. 14. Selected 1mm reconstruction slices of a 185mm diameter cylinder phantom filled with a uniform F18-water solution. Coincidence trigger coincidence rates (top) - from left to right: 3.3 kHz, 9.4 kHz, 18.5 kHz, and 31 kHz. Circular image artifacts due to rate effect can be observed easily at 31 kHz and 18.5 kHz. The images were corrected for absorption in water. The same 1mm vertical imaging slice from a smaller 135mm diameter cylindrical F18-water phantom which has been normalized (divided) slice-by-slice by the corresponding reconstruction slice from the 185mm calibration cylinder can also be seen (middle). The rate-induced artifacts disappear at about the 10 kHz rate. The same 1mm slice from the 135 mm cylindrical phantom normalized by a high statistics 4 hr. long calibration run with the 185mm diameter cylinder, starting at an 11.5 kHz rate is shown on the bottom left. The profile through the disk demonstrates good uniformity (bottom right).

These images demonstrate how effective the flood correction method can be. Here, a smaller uniform phantom was divided by a larger uniform phantom, which images are shown above in the middle row. Note that the phantoms are very uniform after normalization. The graph on the bottom right demonstrates this uniformity. Thus, the reconstructed images from the large phantom above are then used to correct phantom images on a slice by slice basis to achieve uniformity (Fig. 14).
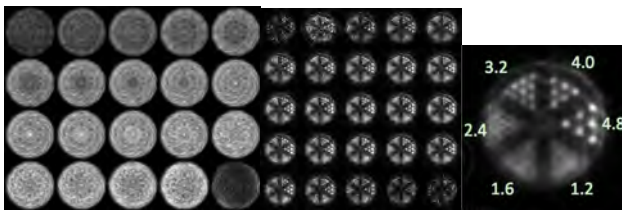
H. Studies with Phantoms

Fig. 15. Twenty 1 mm slices obtained with the uniformity phantom. During reconstruction, the images were corrected for 511 keV gamma absorption in water. The pattern of artifacts in each slice is different and is a reflection of the detector's modular structure and vertical non-uniformity (left). Twenty-five reconstructed Derenzo phantom 1mm slices, corrected for absorption (middle). Sum of the 15 central slices (right).

The Derenzo phantom measurements shown in Fig. 15 demonstrate what the Derenzo phantom looks like in 25

individual 1mm slices (middle). Each of these slices were normalized by individual 1 mm slices of the uniform flood phantom shown on the left. It is notable that the flood pattern varies by slice, even in 1 mm intervals, showing the artifacts produced by the geometry.   The final Derenzo assessment occurred by summing the central most 15 slices together after they were already normalized.   Our results indicate a spatial resolution between 2.4 and 1.6 mm.

We also wished to look at how well a realistic brain phantom could look outside of the MRI. Here, we filled the Hoffman brain phantom (Fig. 16, bottom right) with F^{18} water solution and reconstructed with 1 mm voxels. The images are shown below.
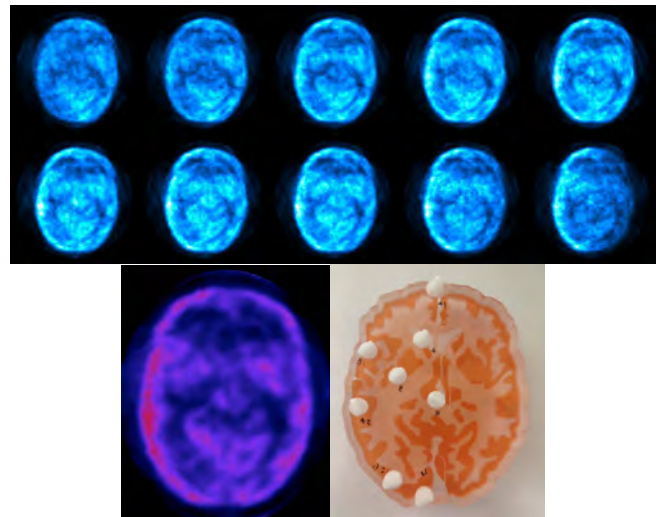

Fig. 16.   Provided here are some examples of the brain phantom images. Ten 1mm thick planar horizontal reconstruction slices (top). One 6mm thick vertical slice of the reconstructed image obtained with the brain phantom at center (left). The physical phantom used for the brain phantom studies (right). The images were normalized by the flood images from Fig. 15.

I. MRI-Operation

As expected, the large body coil placed outside the PET ring was not as efficient in screening the MRI operation from the electrical noise induced by PET as the smaller coil placed inside the ring between the detectors and the phantom (data not shown, concepts can be seen in Fig 17). For phase II we will use shielded cabling which should greatly reduce this pickup. Despite this issue we were able to acquire the PET images simultaneously with the MRI images (Fig. 20). In the event that the phase II imager does not permit simultaneous imaging, it would still be quite useful to image in sequential mode before or after the MRI without moving the patient. In summary the pilot results of these *very preliminary* MRI studies are very encouraging – the MRI images showed only a small loss in S/N, while the PET images seemed to be minimally impacted.   In phase II we plan to study proper shielding of the cables and electronics to minimize this interference.

Fig. 17. Preliminary study of the approach to use standard flexible RF coils to minimize the effect of active PET on MRI. Imaging with the 3T Flex Large flexible RF coil with coil inside PET ring (far left). A flexible coil placed outside the ring in a complementary imaging study (middle right). The experimental setup with the PET ring placed inside the 3 Tesla Siemens MRI (far right). An image of a brain phantom filled with water with a 3T Flex RF coil placed between the brain phantom and the PET ring (middle left). *The PET system was fully powered during imaging.*
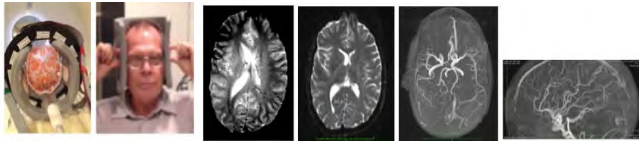

Fig. 18. An MRI scan using a flexible coil with the PET ring. Standard Siemens 3T Flex Large flexible RF coil placed between the brain phantom and the WVU Helmet_PET ring prototype (left). The coil is large enough to cover most of the patient's head, leaving only a small opening for the face (second from left). Four examples of MRI images in a volunteer obtained with the flex coil, showing that the quality of images is mostly undistrubed. Images are (left to right): AX_T2_HEMO, AX_DWI, and twice TOF_3D_multi-slab.
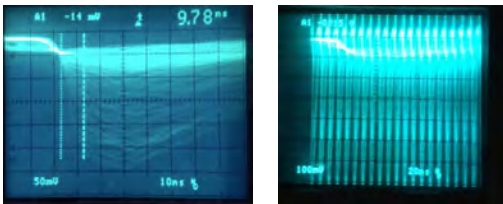

Fig. 19. Pulse shapes of the sum signals measured with a Na22 source at the input to the trigger box (Mesytec) when the ring was mounted inside the MRI scanner. Image when MRI was not running (left). Image when MPRAGE RF pulse sequence was running (right). Even though there is a large amount of induced noise, one can still see the undisturbed PET signals behind the pulses which indicates that the noise is from the cables and not in the SiPMs or electronics.
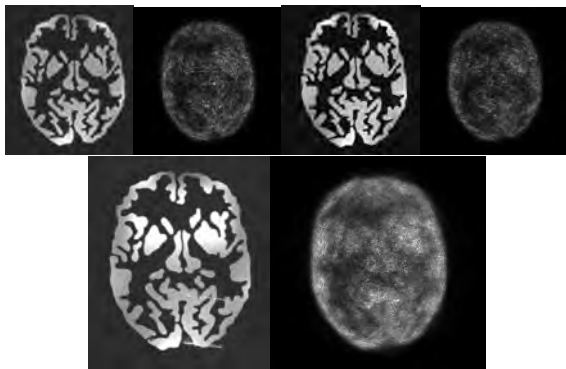

Fig. 20. A preliminary study with simultaneous PET/MR imaging using brain phantoms. Approximately 100 microCurie activity of F18-FDG water solution was in the phantom in the beginning of the series of tests. These particular images are presented with the MR image right next to the associated PET image. From left to right to bottom (with measurement time in brackets): T1 (1min 46 sec), T2 (1min 53 sec), and MPRAGE (8min 40 sec).

V. CONCLUSIONS

We have built and tested the first fully wearable brain PET imaging insert and demonstrated its operation with a radioactive phantom during a simultaneous PET/MRI scan. The results presented in this study can serve as a base for the development of an efficiency-optimized two-three ring PET brain imager that can be used as an MRI insert during simultaneous brain imaging acquisitions. Another implication of our results show that such an imager could operate with a reduced injected dose of a radiolabeled compound, as the current imager due to its close geometry requires only about 10% of the standard dose, as indicated in our rate capability tests. Our speculation is that even doses as low as 1-10% of the standard dose (typically at a 10 mCi level) of an imaging agent such as F18-FDG will suffice to obtain useful images with such an optimized scanner. Naturally, this is assuming that spatial resolution would not be the main focus of such a scan, but rather the basic pattern of metabolic activity. Although not useful for detecting small lesions, this type of imaging could be extremely beneficial in the investigation of neurodegenerative diseases, stroke, brain damage, and trauma and therefore greatly improve the quality of *in-vivo* imaging in numerous different applications. We intend to build a second generation device of this type, with more brain coverage and higher efficiency in the coming years.

REFERENCES

[1] B. Ganguly, N. Mondal, M. Nandy and F. Roesch, "Some physical aspects of positron annihilation tomography: A critical review," *J. Radioanal. Nucl.*, vol. 279, no. 6, pp. 685-698, 2009.

[2] S. Surti, A. Kuhn, M. E. Werner, A. E. Perkins, J. Kolthammer and J. S. Karp, "Performance of Philips gemini TF PET/CT scanner with special consideration for its time-of-flight imaging capabilities," *Journal of Nuclear Medicine*, vol. 48, no. 3, pp. 471-480, 2007.

[3] F. Nishikido, A. Tachibana, T. Obata, S. Yoshioka, N. Inadama, E. Yoshida, H. Tashima, M. Suga, H. Murayama and T. Yamaya, "Feasibility study for a PET detector integrated with an RF coil for PET-MRI," Presented at IEEE Nuclear Science Symposium and Medical Imaging Conference (NSS/MIC), *IEEE NSS Conference Record, M13-7*, 2011.

[4] S. Gomi, H. Hano, T. Iijima, S. Itoh, K. Kawagoe, S. Kim, T. Kubota, T. Maeda, T. Matsumura and Y. Mazuka, "Development and study of the multi pixel photon counter," *Nuclear Instruments and Methods in Physics Research Section A: Accelerators, Spectrometers, Detectors and Associated Equipment*, vol. 581, no. 1, pp. 427-432, 2007.

[5] K. J. Hong, Y. Choi, J. Kang, W. Hu, J. H. Jung, B. J. Min, Y. H. Chung and C. Jackson, "Performance evaluation of a PET detector consisting of an LYSO array coupled to a 4× 4 array of large-size GAPD for MR compatible imaging," *Journal of Instrumentation*, vol. 6, no. 5, pp. P05012, 2011.

[6] J. Kang, Y. Choi, K. J. Hong, J. H. Jung, W. Hu, Y. S. Huh, H. Lim and B. Kim, "A feasibility study of photosensor charge signal transmission

to preamplifier using long cable for development of hybrid PET-MRI," *Med. Phys.*, vol. 37, pp. 5655, 2010.

[7] J. H. Jung, Y. Choi, K. J. Hong, J. H. Kang, W. Hu, B. J. Min, Y. S. Huh, S. H. Shin, H. K. Lim and D. S. Kim, "MR compatible brain PET using tileable GAPD arrays," Presented at IEEE Nuclear Science Symposium and Medical Imaging Conference (NSS/MIC), *IEEE NSS Conference Record, M13-27*, 2009.

[8] J. Ho Jung, Y. Choi, K. Jo Hong, W. Hu, J. Hoon Kang, B. Jun Min, S. Han Shin, H. Keong Lim, Y. Suk Huh and E. Kim, "Development of a position decoder circuit for PET consisting of GAPD arrays," *Nuclear Instruments and Methods in Physics Research Section A: Accelerators, Spectrometers, Detectors and Associated Equipment*, vol. 621, no. 1, pp. 310-315, 2010.

[9] S. Yamamoto, M. Honda, K. Shimizu and M. Senda, "Development of PET-hat: Wearable PET system for brain research," *J. Nucl. Med.*, vol. 50, pp. 1532, 2009.

[10] S. Yamamoto, M. Honda, T. Oohashi, K. Shimizu and M. Senda, "Development of a brain PET system, PET-hat: A wearable PET system for brain research," *IEEE Transactions on Nuclear Science,* vol. 58, no. 3, pp. 668-673, 2011.

[11] S. Majewski and J. Proffitt, "Compact and mobile high resolution PET brain imager," U.S. Patent 7,884,331, 2011.

[12] P. Dokhale, R. Nagarkar, R. Robertson, M. McClish, C. Stapels, J. Christian, G. Entine, M. Squillante, S. Cherry and K. Shah, "Performance measurements of CMOS SSPM as PET detector," Presented at IEEE Nuclear Science Symposium and Medical Imaging Conference (NSS/MIC), *IEEE NSS Conference Record, M14-6,* 2007.

[13] J. Proffitt, W. Hammond, S. Majewski, V. Popov, R. Raylman and A. Weisenberger, "Implementation of a high-rate USB data acquisition system for PET and SPECT imaging," Presented at IEEE Nuclear Science Symposium and Medical Imaging Conference (NSS/MIC), *IEEE NSS Conference Record, M14-123*, 2006.

[14] J. Proffitt, W. Hammond, S. Majewski, V. Popov, R. Raylman, A. Weisenberger and R. Wojcik, "A flexible high-rate USB2 data acquisition system for PET and SPECT imaging," Presented at IEE Nuclear Science Symposium and Medical Imaging Conference (NSS/MIC), *IEEE NSS Conference Record, J03-52*, 2005.

[15] J. McKisson, W. Hammond, J. Proffitt and A. Weisenberger, "A java distributed acquisition system for PET and SPECT imaging," Presented at Nuclear Science Symposium and Medical Imaging Conference (NSS/MIC), *IEE NSS Conference Record, M18-342*, 2007.